The proximity focusing RICH

Requirements

Requirements from physics: Particle identification capabilities in the electron going endcap region of the ePIC detector ($-3.5 \leq \eta \leq -1.5$) will be provided by a proximity focusing ring imaging Cherenkov detector (pfRICH). Driven primarily by the requirements from SIDIS measurements, the pfRICH will need to provide 3σ separation or better between pions, kaons, and protons for momenta $p < 7$ GeV/c. The pfRICH will also play a critical role in electron-hadron separation for momenta below roughly 3 GeV/c, where hadron distributions are at their maximum and the electron ID capabilities of the backward EM calorimeter will not be sufficient to achieve the overall required electron purity. In addition to electron and hadron identification, the excellent timing resolution of the pfRICH photosensors, High Rate Picosecond Photon Detectors (HRPPDs), will allow the pfRICH to provide a high quality t_0 reference for the barrel and forward endcap time-of-flight detectors.

Requirements from Radiation Hardness: The beam induced charged particle background impacts the pfRICH mainly via excess photons produced in the aerogel and fused silica windows of the HRPPD photo sensors. A fraction of the incoming photons are converted to photo-electrons (PE) by the photocathode according to its quantum efficiency. The amplification of PEs due to a secondary electron emission in the MCPs desorpts ions off the micro-channel walls. These ions drift towards the photocathode, and can react with or even sputter the photocathode material which leads to degradation of its quantum efficiency. HRPPD gain can also be affected due to a degradation of the secondary emission layer.

To estimate the flux of ion back flow during the expected life span of the detector, a simulation study was performed, combining the rates from DIS events and beam gas interactions. A mass-dependent minimum energy cutoff was applied so that only particles that would produce Cherenkov radiation in the aerogel plane or HRPPD window would be considered. Each particle producing Cherenkov photons in the aerogel (n = 1.04) was assumed to produce ≈ 10 photoelectrons, while ≈ 100 photoelectrons were assumed from the HRPPD window (n = 1.45) after factoring in the QE.

Convoluting an expected operating gain of 10^5 with a running period of 26 weeks/year and a luminosity of 10^{34} cm^{-2}s^{-1} yields a yearly estimate for accumulated charge of up to 0.011 C/cm^2 on the photocathodes of sensors closest to the beam line. For a running period of 10 years, this will result in 0.11 C/cm^2, or 1.1 C/cm^2 if one assume a higher gain of 10^6 to compensate the aging over time. It should be noted that the estimate of particle flux is based on realistic simulations for beam gas and DIS events. Furthermore, the rates and running period are overestimated which gives a safety factor of around 2 from the most plausible scenario. Studies to evaluate the degradation of QE with the accumulated charge are underway.

Requirements from Data Rates: Estimations of the expected data rates for the pfRICH were made using the same DIS + beam gas simulations that were used for the radiation hardness studies. The hit rates from physics and background sources as well as a noise rate of 2.34 MHz per HRPPD leads to a digitized data rate of 45 Gb/s for the entire detector. This is not divided evenly over all HRPPDs as those closest to the beamline see higher particle fluxes. The largest data rates per HRPPD are 1.5 Gb/s while the smallest are 205 Mb/s. These rates are not expected to pose a problem for the front-end electronics or data acquisition system.

Justification

Device concept and technological choice: The operation of a generic proximity focusing RICH detector is based on a very simple set of principles. A charged particle passing through a thin layer of radiator (often aerogel with an appropriate refractive index) with a velocity higher than the speed of light in that medium emits Cherenkov light (photons) at an angle which is solely determined by the particle mass, momentum, and refractive index of the radiator. The 3D momentum of the particle is typically provided by a tracking system. If the average refractive index of the radiator is also known, measurements of the Cherenkov light emission angle can determine the particle mass, thus allowing identification of different particle species, e.g. distinguishing electrons, pions, kaons, and protons.

The ePIC pfRICH was designed as a conceptually simple detector, based on proven principles, providing a high degree of performance that is practically uniform over the whole available angular acceptance in η and ϕ. In order to reach the performance requirement of 3σ separation or better of $\pi/K/p$ for momenta $p < 7$ GeV/c, the pfRICH design was optimized in the following ways: (1) the proximity gap length was maximized as much as possible within the volume available in ePIC; (2) the radiator thickness was taken to be small enough to reduce the contribution to the single photon angular resolution to below $\sim$5 mrad, yet produce enough photons per track to robustly reconstruct the Cherenkov angle; (3) the HRPPD pixellation was chosen such that it contributes at most $\sim$2 mrad to the angular resolution; and (4) the acrylic filter cuts off all UV light produced in the aerogel below $\sim$ 300 nm, where the $dn/d\lambda$ dependency is strongest. In addition to satisfying the PID requirements in the backward direction, the small material budget of the pfRICH design minimizes the impact on the energy resolution of the endcap electromagnetic calorimeter which sits directly downstream.

Subsystem description:

General device description: The layout of the proposed ePIC pfRICH detector is shown in Fig. 1. It consists of a 1.3 m diameter and $\sim$49 cm long cylindrical vessel with the outer and inner walls made from a lightweight honeycomb carbon fiber sandwich and front and rear plates made of a carbon fiber reinforced plastic (CFRP). The vessel sits 123.6 cm from the nominal interaction point. Forty-two 2.5 cm thick

aerogel tiles of a trapezoidal shape are installed in individual opaque compartments in a container mounted on the upstream side of the vessel. A thin acrylic filter is installed immediately after the aerogel container. The vessel is continually flushed with dry purified nitrogen. Sixty eight HRPPD photosensors are installed in individual slots in the rear CFRP mounting plate with their fused silica windows facing the aerogel. Inner and outer conical mirrors cover the cylindrical sides of the vessel in order to increase the η acceptance of the Cherenkov photons produced in the aerogel radiator. Readout boards equipped with four 256-channel EICROC ASICs are mounted on the rear ceramic anode plates of each of the HRPPDs.

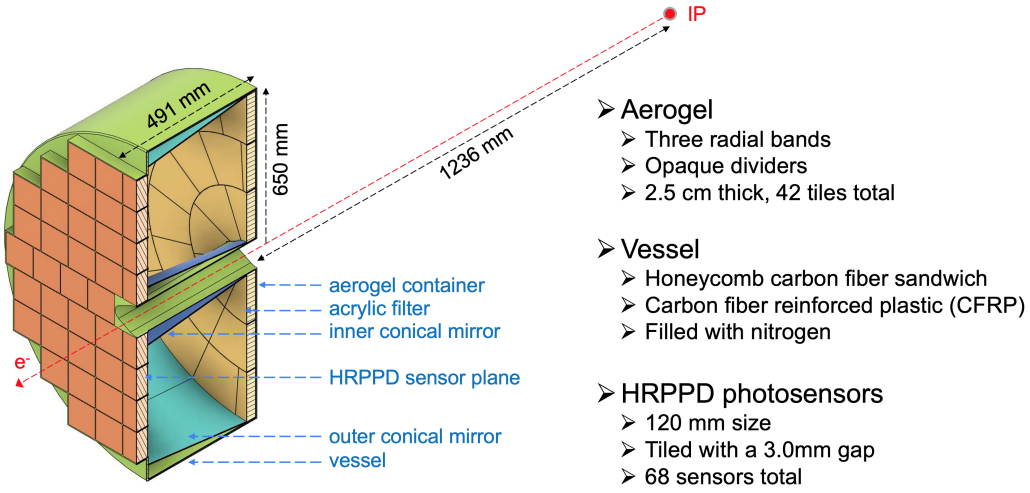

Figure 1: The proposed pfRICH detector. See the text for more details. (Figure documentation)

Sensors: An improved version of the Micro-Channel Plate Photomultiplier Tubes (MCP-PMTs) manufactured by Incom Inc. [1], the so-called High Rate Picosecond Photon Detectors (HRPPDs), will be used as the photosensor solution, see Fig. 2.

The sensor dimensions will be 120 mm x 120 mm, with a 104 mm x 104 mm fully efficient active area in the center (75% geometric efficiency) and will have slightly tapered 5 mm thick UV-grade fused silica windows. A DC-coupled variety of these sensors will be used, with the inner side of the anode base plate patterned into 32 x 32 square pixels, corresponding to 1024 channels per sensor, and a pitch of 3.25 mm. The sensors will be equipped with a UV-enhanced high quantum efficiency (QE) bialkali photocathode, with peak values exceeding 30% at 365 nm (see left and center panels in Fig. 3) [2]. The HRPPDs will be fitted with a pair of 600 μm thick MCPs with a pore diameter of 10 μm, open area ratio in excess of 70%, and bias angle of 13 degrees in a conventional chevron configuration. These will be operated at an amplification voltage of up to $\sim$700 V to comfortably achieve an overall detector gain above 10^6 if needed. The anode base plates will be manufactured from multi-layer High Temperature Co-fired Ceramic (HTCC) by Kyocera (Japan). They will have a custom design, matching the uniform 32 x 32 pixellation on the inner (vacuum) side

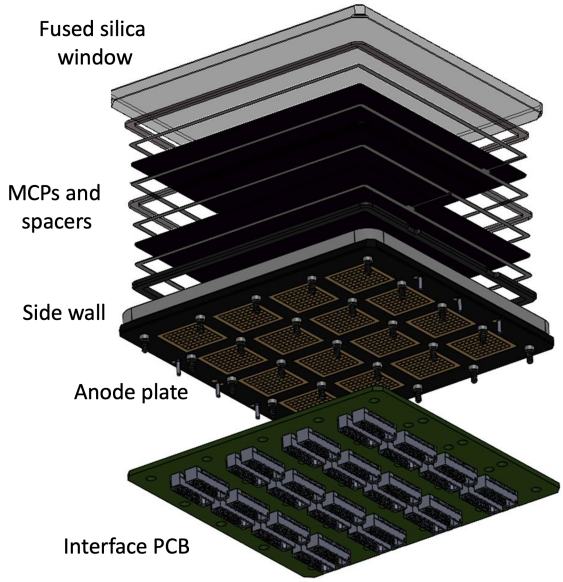

Figure 2: HRPPD photosensor CAD model with a passive interface board. Compression interposers between anode base plate and this PCB are not shown. (Figure documentation)

of the sensor, short shielded traces inside of the ceramic stack, and a pattern of square pads with a smaller pitch on the outer side, matching the readout PCB design.

HRPPDs have a demonstrated single photon Transit Time Spread (TTS) of ∼20 ps or better (right panel of Fig. 3). They have very low dark count rates (DCR), not exceeding few hundred Hz per square centimeter at a gain of 10^6 (see [3], slide 10). HRPPDs are expected to perform well in a 1.3 T magnetic field at the location of the pfRICH sensor plane in ePIC. Direct measurements will be performed in 2025, however the recent studies of LAPPDs with 10 micron pore MCPs indicate that HRPPD gain in a 1.3 T field should be recoverable to at least the level of 10^6 by increasing the MCP bias voltage [4].

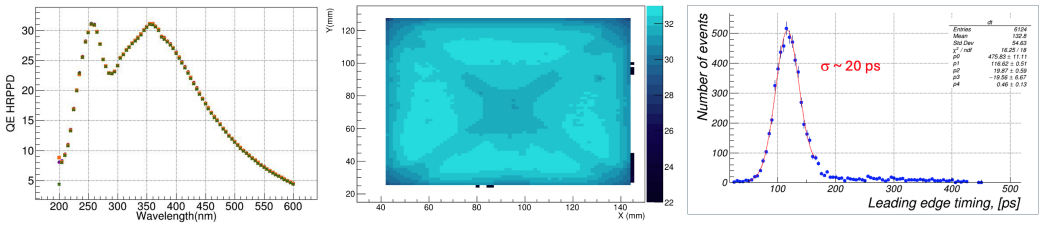

Figure 3: Left: EIC HRPPD QE as a function of wavelength. Center: QE map in the full active area at a wavelength of 365 nm. Right: Single photon timing resolution measured using Elmo 780 femtosecond laser with a wavelength of 390 nm. (Figure documentation)

FEE: Each sensor will be equipped with four 256-channel EICROC ASICs [5], designed by the OMEGA group [6], each serving one quadrant of the sensor. EICROC

ASICs will be built via a 130 nm technology process, with an expected power consumption of 1-3 mW/channel [5]. They will provide a Time of Arrival (TOA) and an ADC measurement with a dynamic range of 1 pC for each pixel, which should be sufficient for both single photon hits (both imaging and timing) and multi-photon hits (timing only) at a moderate HRPPD gain of a few times 10^5. The ASICs will be able to measure the TOA with a resolution better than 20 ps per pixel assuming detector capacitance on the order of $\sim$10 pF, leading edge length of the HRPPD signal below 500 ps, and collected charge of a few dozens fC achieved by tuning the MCP gain [6]. These ballpark parameters seem to be easily within reach for pfRICH HRPPD sensors.

The ASICs will be bump bonded to the readout PCB in a "flip-chip" fashion to minimize the parasitic capacitance of the traces inside of the PCB stack. Preliminary estimates show that in such a scheme, where four 16 x 16 primary pixel arrays with a pitch of 3.25 mm are first "compressed" to a 2.0 mm pitch inside the HRPPD ceramic base plate and then further reduced to a 500 μm pad size in the readout PCB stack in order to ultimately match the EICROC ASIC pitch, the combined pad and trace capacitance should not exceed 10 pF. This is well within the expected operating range of the ASICs.

Each ASIC will be connected via a dedicated copper link to its respective readout unit (RDO), located on the outer circumference of the rear side of the pfRICH vessel. Each RDO will serve 16 EICROC ASICs, for a total of 17 RDOs. The RDOs will then be connected to a single Data Aggregation Module (DAM). The DAM board is envisioned to be a FrontEnd LInk eXchange (FELIX) board [7] installed in the DAQ. The RDO will be connected to the DAM via a high speed optical link capable of at least 5 Gb/s throughput. The RDOs will follow the same design used by the ePIC pixelated AC-LGAD detectors. These boards will utilize lpGBT for aggregation of ASIC data and VTRX+ to provide the fiber interfaces. The RDO should deliver timing signals synchronized to the beam crossings with jitter $<$ 5ps.

Other components: In addition to the vessel structure and sensors described above, two other components will be critical to the pfRICH: the aerogel radiators and mirrors. The pfRICH will be equipped with aerogel tiles produced by Chiba Aerogel Factory Co., Ltd. [8] with a nominal refractive index, $n \sim 1.040$ and a thickness of 2.5 cm. The aerogel will be cut using a water jet technique into trapezoidal tiles providing a required radial and azimuthal segmentation with minimal dead area. This type of aerogel will replicate the performance of the material used in the Belle II experiment [9], and in particular, will be very transparent in the near UV range, with an absorption length and Rayleigh scattering length in excess of 5 mm down to $\sim$275-300 nm. The aerogel tiles will be installed in segmented containers (slots) with $\sim$500 μm thick walls and held in place with a thin filament. The container walls will be opaque to suppress stray photons leaking out of the aerogel tile side facets, which are not expected to be of a high optical quality after water jetting.

The pfRICH will also utilize three types of mirrors to increase the active acceptance of the detector. The outer mirror cone consists of 12 segments approximately 40 cm in length which sit just inside the outer wall of the pfRICH vessel. These mirrors will

recover Cherenkov photons from charged particles with large polar angles which pass through the aerogel but would exit the vessel before reaching the sensor plane. Similarly, a set of inner mirrors which wrap around the beam pipe and surrounding support structures will reflect photons emitted by small angle charged particles (close to $\eta \approx -3.5$) back onto the sensor plane. Finally, small pyramidal mirrors will be placed on top of the HRPPD side walls to reflect (funnel) photons hitting this area back into the sensor acceptance. The mirrors themselves will have a reflectivity of approximately 90% for wavelengths between 300 and 600 nm and will be produced at Stony Brook University using an evaporator with the CFRP substrate material provided by Purdue University.

Performance

Monte-Carlo simulations: The performance of the pfRICH design was studied using a custom simulation and reconstruction software suite. The geometry of the detector, along with other relevant characteristics such as the ePIC magnetic field map, aerogel optical properties, mirror reflectivity, and HRPPD quantum efficiency were modeled in GEANT4 v10.05.p01 [10]. The reconstruction made use of the Inverse Ray Tracing (IRT) library, which is part of the ePIC software stack [11], and a ROOT [12] based data structure providing access to all photo-electron, track, and event level quantities.

Parameters relevant to the performance of the pfRICH were determined by simulating single particles thrown at a variety of energies and angles. On average, roughly 11 Cherenkov photons were detected from particles at the saturation momentum, which is in agreement with first principles estimates taking into account a realistic sensor quantum efficiency. The working acceptance of the detector, defined as the region in which the ratio of tracks producing at least one detected photon over the total number of tracks is greater than 80%, was found to cover $-3.5 < \eta < -1.5$. Single photo-electron (SPE) and track level resolutions in the working acceptance were also determined, with the SPE resolution being roughly 5 mrad and independent of momentum, while the track level resolution improved with the number of detected photons and reached a value of 1.7 mrad.

The algorithm for event based reconstruction of the Cherenkov angles was validated using multi-particle simulations. The reconstructed Cherenkov angle (in units of mrad) as a function of particle momentum (in units of GeV/c) is shown in the left panel of Fig. 4 and compared to the theoretical expectations for a given mass hypothesis. It is seen that the reconstructed angles and theoretical expectations are in good agreement, confirming that the event based reconstruction is performing well. This plot also shows that the Cherenkov saturation angle is approximately 295 mrad. The N_σ separation count between the electron-pion and pion-kaon hypotheses as a function of momentum are shown in the middle and right panels of Fig. 4, respectively. It is seen that 3σ separation is possible up to roughly 2.5 GeV/c for electron-pion and 9 GeV/c for pion-kaon hypotheses. Performance was found to be relatively uniform across the whole acceptance of the detector.

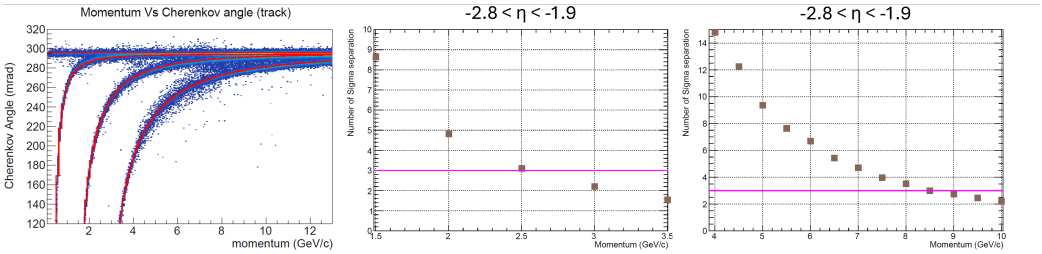

Figure 4: (Left) The reconstructed Cherenkov angle for electrons, pions, kaons, and protons as a function of momentum. (Middle) N_σ separation between the electron and pion hypotheses as a function of momentum. (Right) Same as the middle panel, for pion and kaon hypotheses. (Figure documentation)

One of the main purposes of the pfRICH detector is to identify low momentum scattered electrons in the backward direction. Specifically, it will help with separating the electrons from π^- mesons, which are expected to dominate in the pfRICH acceptance. Using PYTHIA-6 e+p collisions at 18 $\times$ 275 GeV, it was shown that the pfRICH will provide good π^--electron separation for $p < 2$ GeV/c and decreasing separation power for momenta up to $\sim$ 5 GeV/c as seen in the left panel of Fig. 5. The pfRICH detector therefore plays an important role in the ePIC detector, allowing identification of the scattered electrons in kinematic region not accessible by other detectors.

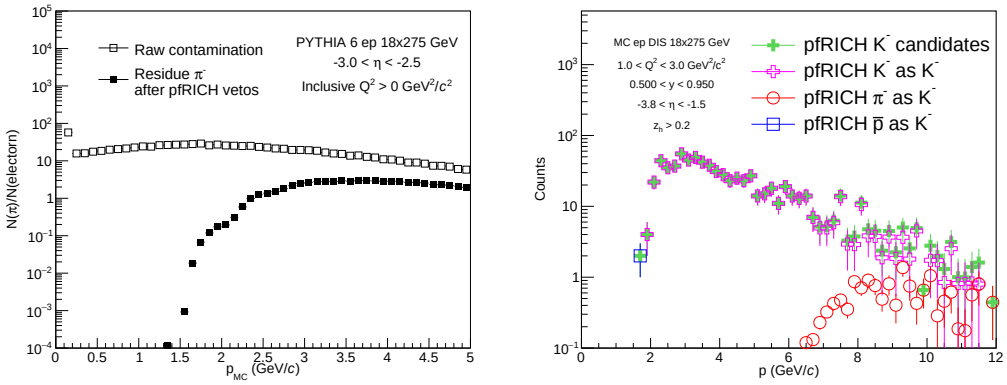

Figure 5: (left) Yield ratio of π^-/e_{scat} before (open black squares) and after (black full squares) pfRICH veto on π^- in PYTHIA 6 e+p collisions at 18$\times$275 GeV for $-3.0 < \eta < -2.5$. (right) Kaon candidates identified using the pfRICH (full markers) in MC DIS e+p collisions at 18 $\times$ 275 GeV in PYTHIA 8. The open markers show contributions from correctly identified kaons and other hadrons misidentified as kaons. (Figure documentation)

Another important utilization of the pfRICH is hadron identification in the backward region in SIDIS studies. For that reason, the ability to separate π, K, and p hadrons was studied using simulation of e+p collisions at 18 $\times$ 275 GeV in PYTHIA 8. Specifically, the expected purity of leading K^- mesons was evaluated and was shown to be close to 100% up to hadron momenta of $p < 6\,\text{GeV}/c$, as shown in the right panel of

Fig. 5. This means that pfRICH will play an important role in SIDIS studies as it can efficiently distinguish various hadron species in a wide momentum range.

Timing performance: A primary use of the excellent HRPPD timing resolution is providing an independent t_0 reference to the barrel and forward endcap Time of Flight subsystems. However, one can make use of the t_0 $\sim$20 ps reference provided by the accelerator, and apply Time of Flight techniques to the pfRICH as a standalone subsystem. This functionality is built into the Inverse Ray Tracing reconstruction algorithm (IRT 2.0) already, for both ambiguity resolution between a variety of photon optical paths for a given pair of emission and detection point candidates, and in a combined particle identification procedure using imaging and timing information at once. Numerical estimates follow, for performance illustration purposes.

The pfRICH aerogel wall and HRPPD sensor plane will be located about 1250 mm and 1650 mm from the IP, respectively, which can serve as a conservative estimate of the flight paths. An energetic charged particle will produce $\sim$10 detected Cherenkov photons in aerogel, and - in cases when it crosses the HRPPD fused silica window - a photon flash resulting in at least a dozen neighboring pads hit. In either case one can conservatively assume that an overall timing measurement will be of a factor of at least 3 higher than the single photon resolution. Even assuming that the HRPPD single photon resolution under real life experimental conditions will be 25-30 ps rather than 15-20 ps as bench studies using a femtosecond laser indicate (see Fig. 3, right), one can come to a conclusion that a standalone pfRICH time of flight measurement will be dominated by the precision of the accelerator t_0 estimate at the IP. If one takes 25 ps as an overall time of flight measurement resolution between the IP and aerogel and HRPPD windows, 3σ separation can be achieved between different particle hypothesis pairs as indicated in Table 1. In particular, one can clearly see that kaons and protons can be resolved at momenta far above kaon Cherenkov threshold in pfRICH aerogel. Therefore, a combined imaging and time of flight technique will provide a positive kaon identification in the whole momentum range, down to few hundred MeV/c.

	aerogel	HRPPD window
e/π separation	up to 0.75 GeV/c	up to 0.85 GeV/c
π/K separation	up to 2.50 GeV/c	up to 2.85 GeV/c
K/p separation	up to 4.20 GeV/c	up to 4.80 GeV/c

Table 1: Expected pfRICH time of flight based particle identification performance. Highest momenta at which 3σ separation for a respective pair of mass hypotheses can be achieved is quoted, for aerogel and HRPPD window radiators separately.

Hardware component evaluation: Hydrophobic silica aerogel manufactured by the Aerogel Factory [8] will be used for the radiator in the pfRICH detector. Three hydrophobic aerogel tiles, with nominal dimensions of 11 cm $\times$ 11 cm $\times$ 2.5 cm, density of 0.14 g/cm^3, and refractive index of 1.04, were ordered from the Aerogel Factory to verify and assess their refractive index and transparency, two aerogel properties which are critical to the detector's performance. The refractive index was determined

at Temple University by measuring the deflection of the refracted light exiting the corners of the aerogel (see QA section). The refractive index measured by Temple University (n_{TU}) and the Aerogel Factory (n_{AF}) were found to be in agreement, with a typical value of $(n_{TU} - n_{AF}) \,/\, (n_{AF} - 1) \sim 2\%$. The optical transparency was evaluated by measuring the transmittance as a function of wavelength. Transmittance curves for each tile were measured by the Aerogel Factory using a monochromator and spectrometer (Hitachi U-4100) [13], at BNL using a monochromator and spectrometer (Hitachi U-3210), and at Temple University using a LED and spectrometer setup which provides measurements at four discrete wavelengths (see left panel of Fig. 6). These three sets of measurements were found to be consistent with each other within the quoted errors. A sufficiently high transmittance of about 68.5% at 432 nm was found when averaging the results from three different measurements over the three produced aerogel tiles at Temple. The wavelength dependent transmittance measurements were used to extract additional information such as clarity, transmission length, and scattering length.

The mirrors will be produced by the pfRICH subsystem collaboration members, with substrates fabricated at Purdue University and coating performed at Stony Brook University. Optimization of the substrate and coating procedures is ongoing with a number of mirror samples being produced with different substrate manufacturing techniques, coating chamber settings, and coating material thickness. The reflectivity of the various mirror samples was evaluated at BNL using a dedicated test stand. The best performing mirror sample, manufactured using a ∼12 kilo-angstrom thickness aluminium coating, showed a measured average reflectivity of 0.89 for wavelengths between 300 and 600 nm (see right panel of Fig. 6).

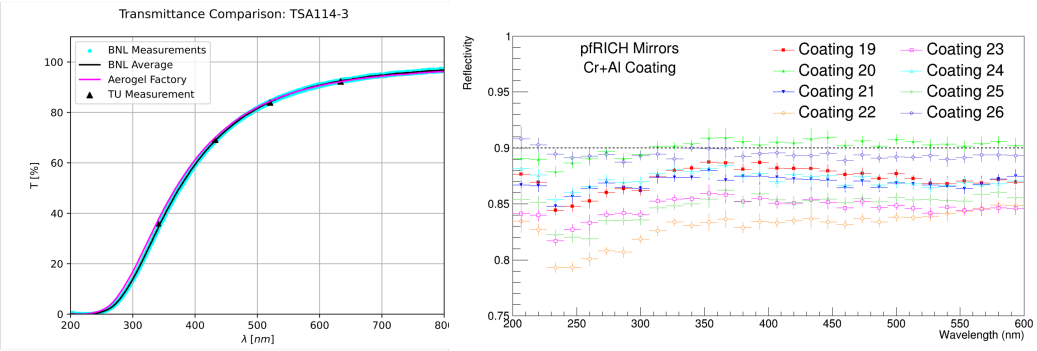

Figure 6: Left: Aerogel transmittance as a function of wavelength for factory, BNL, and Temple University measurements. Right: Mirror sample reflectivities as measured at BNL as a function of wavelength. (Figure documentation)

Implementation

Services: Services relevant for the pfRICH include High Voltage (HV) and Low Voltage (LV) systems to operate the photosensors and power the front-end electronics, respectively,

a cooling system to regulate the temperature of the electronics and sensors, and a gas system to maintain the proper environment inside the pfRICH vessel.

The HV and LV modules will be located on the electronics platform, about 15 meters away from the pfRICH detector, in a low Total Ionizing Dose (TID) environment. Therefore, standard off-the-shelf units can be used. The high-voltage system will consist of 340 individual stackable negative HV channels. Twenty three CAEN A1515BV 16-channel 1.4kV/1mA floating ground modules [14] will be used. The HV modules will be housed in a pair of CAEN SY4527 mainframes [15], equipped with additional 1200 W power module boosters. Each of the twenty three modules will be connected to an enclosed box distribution PCB installed on the rear side of the pfRICH vessel. The box is fed from individual 15 m long multi-conductor high voltage cables. For the HV interconnect, CERN-approved 52-pin Radiall cable connectors and receptacles will be used throughout the system. The distribution PCB will arrange five of the isolated channels of the A1515BV in a manner to provide five individual stacked voltage levels and a common ground referenced return to each HRPPD. The respective five bias levels and ground will be connected to the pads on the rear side of the HRPPDs via narrow profile Teledyne Reynolds shielded 26 AWG coaxial cables, conductive vias in the Front End Board (FEB) stackup with a matching pad pattern, and custom Samtec compression interposers.

The EICROC ASICs will require 1.2 V low-voltage power. Under the assumption of up to 3 mW/channel power dissipation this corresponds to 3 W power (or up to 2.5A current) per photosensor FEB. Accounting for other electronics components present on such a FEB, and providing a 20% safety margin, we estimate the total power consumption to be less than 300 W for the whole system. This number is used as input for designing the cooling system discussed below. We will be using a single Wiener MPOD Mini LX crate with a MPOD-C controller and four MPV4008I1 4-channel LV modules [16]. One Low Voltage channel will serve four FEBs. 15 m long tray rated 10 AWG jacketed cables with 20AWG (sense wires) will run between the electronics platform and a LV distribution panel on the rear side of the pfRICH vessel. From there, 18 AWG multi-conductor cables will distribute power to the individual FEB cards.

The pfRICH cooling system will consist of several off-detector components and a few on-detector thermal interfaces and assemblies. The primary heat dissipating components will be the ASICs, which are anticipated to produce just over 1 W each (4 W per module), or about 300 W for the 68 total modules. In addition to the ASICs, the sensors are anticipated to dissipate just under 1.5 W each or 100 W total. Conservatively, the total power output will be roughly 400 W. Following the geometry, each row of sensors will have its own pair of titanium cooling tubes directly over the ASICs. The pair of tubes that contact the same row of sensors will be in series, and all rows will be in parallel with each other. The tubes will be attached to aluminum plates with thermal epoxy, and a gap pad between the plate and ASIC will maximize thermal contact. Using a stock tube of 0.25" OD and 0.218" ID and maintaining a minimal temperature gradient in the water allows the mass flow rate to be calculated. From there the Reynolds number and pressure drop can be determined, confirming the viability of the system. Additionally, a finite element analysis (FEA) was performed to confirm the water temperature difference and determine the thermal gradi-

ent across the various components. With the described configuration, the sensors reach a maximum temperature of about 32 C in the analysis.

The three primary off-detector elements of the cooling system are a Polyscience chiller, Chilldyne circulator, and a distribution panel. The Polyscience chiller will allow the water to be slightly colder than room temperature, or about 15 C, which is the lowest recommended temperature without nearing the dewpoint in the interaction region. The unit is also capable of flowing about 10 liters per minute (lpm), dissipating about 800 W at that temperature and maintaining the temperature within +/-0.1 C. The Polyscience chiller would be paired with a Chilldyne negative pressure system capable of circulating water at about 8 lpm and $\sim$10 psi. It offers a significant advantage over a positive pressure solution, as if there is a leak in the system, it will draw air into the tube instead of letting water out and potentially damaging electrical components.

The gas system for the pfRICH detector is designed to circulate dry nitrogen at precise pressure and flow rates to remove moisture from within the pfRICH chamber. High-purity nitrogen ($H_2O < 3$ ppm) will be supplied from cryogenic sources. To provide secondary protection, moisture traps such as silica gel dryers will be installed near the nitrogen source. The system will maintain both the required moisture levels and gas purity by ensuring that it is sufficiently gas tight and that the chamber is kept at a slight overpressure (4 mbar) above atmospheric pressure, preventing any infiltration of ambient air. A 0.5 μm filter will be added near the source to capture dust particles. A standby nitrogen source will be available to ensure continuous operation in the event of a primary source failure. To manage fluctuations in the source pressure, a digital pressure outlet controller will be used. Additionally, nitrogen flow will be regulated by a non-pressure-limiting digital mass flow controller. The nitrogen flow rate is expected to allow several complete volume exchanges per hour, with the precise rate to be finalized later.

Pressure inside the chamber will be controlled using a tank blanketing pressure regulator, which maintains a positive internal pressure relative to varying atmospheric conditions. An overpressure protection bubbler will serve as a safeguard against excessive pressure within the chamber. To ensure uniform nitrogen distribution and prevent localized air pockets, nitrogen will be introduced into the chamber at two locations near the top side of the pfRICH vessel, closer to the aerogel plane, and exhausted through two openings near the sensor plane at the bottom. All exhausted gases will be vented outside the experimental area. The entire gas system will undergo pressure testing at 1.5 times the operating pressure to ensure integrity. For monitoring and troubleshooting, pressure gauges and transmitters will be installed, with critical data such as chamber pressure and flow archived for reference.

Subsystem mechanics and integration: The shell that creates the volume of the detector will be made primarily of carbon fiber to optimize the radiation length in ePIC. Specifically, the sensor plane is intended to be made from a bulk carbon fiber layup at approximately 14.7 mm thick at its thickest point. The bulk carbon fiber will be molded and CNC-cut to allow for individual sensor frames and staves to be bonded in-place to create 68 sensor pockets along this plane of the detector. Each individual HRPPD sensor will be added into

the sensor plane from the outside of the vessel and sealed in each of the sensor pockets with a face seal. The overall plane will be sealed to the cylinder at the outer and inner walls using a tightly spaced bolt-pattern and an o-ring groove on the upstream end of the sensor plane to accommodate another face seal.

On the upstream end of the vessel, the aerogel plane will be made from a carbon fiber honeycomb layup around 1/4" thick. The outer and inner circumferences of the aerogel plane will house a sealing ring made from bulk carbon fiber and an o-ring groove to create a face seal. Attached to this aerogel plane will be a web of carbon fiber that creates radial rows of pockets for the aerogel to be placed in. These tiles will be held into the pockets using a thin transparent line strung across the opening in order to contain them in place.

The cylindrical portion of the vessel consists of identical end rings on the upstream and downstream end that house the threaded bolt holes and sealing surfaces for the sensor plane and aerogel plane face seals. These end rings are approximately 3/4" (on the bolting surface) and 1" in thickness (in the z-direction). They are made from bulk carbon fiber and contain threaded inserts that are placed by CNC-machining the insert locations and bonding and threading them into place. The rest of the cylinder is made from single sheets of carbon fiber on the inside and outside of the vessel, as well as a 3/4" nomex honeycomb layer in between.

The inner wall of the cylinder is created in a similar manner to the outer wall, namely a honeycomb construction with the end rings embedded into both ends for bolting and sealing to the aerogel and sensor planes. However, the shape of the inner wall is made such that there is 5 mm of clearance (radially) from the beam pipe flange that the pfRICH will need to pass by to be installed in ePIC. This makes the shape of this inner wall similar to an egg or an avocado.

Lastly, the conical mirrors are designed such that they are attached solely to the sensor plane. This is being done to ensure that the mirrors can be controlled in relation to the sensors and will be unaffected by manufacturing misalignments and tolerance stack-up issues throughout the rest of the vessel. As such, they will hang cantilevered perpendicular the sensor plane for both the inner and outer mirrors. The outer mirrors will be concave and the inner mirrors will be convex. The construction will be a combination of a molded, bulk carbon fiber base with a bonded lexan sheet on top of it (which will have been deposited with a mirror film).

Once the pfRICH has been fully assembled and ready to be placed in the overall ePIC detector, it will be moved around the assembly hall on a cart. The cart will integrate lifting eyelets for the installation of the pfRICH into ePIC, rails identical to its final location, and wheels to transport, store and work on the detector when it is out of the barrel. This tooling will allow us to lift the cart with the pfRICH secured in place with the crane in the detector hall, position it against the barrel, align the rails, and transfer the pfRICH into its final position by translating it along the z-axis.

Calibration, alignment and monitoring: A laser-based system will be used to monitor the pfRICH performance throughout its operational life. The purpose is to monitor, on

a pixel-by-pixel basis the single photon timing resolution, the single photon pulse hight amplitude (HRPPD gain), HRPPD QE, and the relative delays between channels on a few ps level. The system will also monitor the reflectivity of the conical and pyramidal mirrors. To measure the timing resolution, an array of six fibers is introduced inside the detector volume from the aerogel side which casts a broad profile of low-intensity light onto the sensor plane such that each HRPPD pixel accumulates some number of single photon hits after a given number of laser pulses. The distance between a given fiber tip and an HRPPD pixel (minimum of 40 cm) defines the flight time for photons emitted from this fiber, hence the distribution of reconstructed flight times will reveal the timing resolution for this single pixel. Similarly, a separate array of six fibers is arranged such that emitted photons reflect off of the outer mirror surface before impinging on the HRPPDs. In this case, the single photon counting rate is monitored for any degradation over time, which would indicate the deterioration of either the photocathode quantum efficiency or mirror reflectivity, or both.

The pfRICH monitoring system deploys a picosecond PiLas laser which produces a 405 nm laser beam with a nominal $\sim$ 45 ps pulse width. The beam is coupled to a custom 1-to-14 optical fiber splitter by Thorlabs, that evenly distributes the light into arrays of fibers routed into the detector vessel. Two additional fibers are connected to silicon photodiodes to provide laser signal quality verification and an initial timestamp (t_0). A custom-sized 5 mm $\times$ 5 mm engineered diffuser is used to generate a uniform 50° square pattern to optimize the intensity profile emitted from each fiber. Additionally, a fiber delay line is added to each fiber branch to provide the ability to easily separate out in time photons originating from a given fiber. In all, there are three sets (segments) of fibers downstream of the splitter that deliver photons from the laser to the detector vessel: delay fibers, long extension fibers, and fibers mounted permanently inside the detector vessel. Finally, multiple fast photodiode sensors are used to sample the laser light before and after the splitter to monitor the light output intensity and the timing performance.

A relative alignment of the conical mirror segments inside of the vessel, and surface mapping will be performed on a fully assembled detector (up to the front wall removed) prior to the installation in ePIC, by using a 3D scanning system which is being built now for the purposes of first article mirrors QA assessment. The vessel as a whole will be aligned in ePIC after the installation, following a generic procedure developed by EIC engineers for all detector subsystems. Appropriate survey targets will be mounted on the rear and barrel sides of the vessel if required.

Status and remaining design effort: As shown in the previous text, the present pfRICH design fully meets the EIC Yellow Report requirements and subsequent amendments (see performance section):

- Pseudorapidity coverage from -3.5 to -1.5 in the electron-going endcap
- π/K separation on a 3σ level up to 7 GeV/c in this whole acceptance
- $\sim$20 ps timing reference for ePIC ToF subsystems in the barrel and the forward end-

cap by combining single photon signals from aerogel and signals from multi-photon flashes of Cherenkov photons produced by charged particles in HRPPD fused silica windows

R&D effort: The pfRICH design is based mostly on proven technologies, therefore, the remaining R&D effort is fairly small. FY25 R&D activities (partly funded through eRD110 consortium) will be limited to HRPPD aging studies, which will be performed at JLab and INFN Trieste.

E&D status and outlook: Several engineering design activities and first article productions described earlier in the text in more detail have been performed in FY24, and will continue into FY25:

- Full size mirror production and quality assessment
- First article pfRICH vessel outer shell production
- Adjustments of the production process of CFRP-based parts, mirror substrates and HRPPD pockets in the sensor plane in particular
- Fine tuning of the aerogel refractive index and bulk uniformity measurement procedure
- HRPPD sensor design modifications required after the first batch was produced
- HRPPD performance confirmation in the $\sim$1.3 T magnetic field typical for a pfRICH location in ePIC

Other activity needed for the design completion: The readout backplane design cannot be fully completed at this stage because of the unavailability of a final design iteration of the anticipated ASIC chip (EICROC) in either of its low channel count configurations (64, 128 or 256 channels).

The performance of the pfRICH in its anticipated configuration needs to be confirmed in a beam test for both Cherenkov photon imaging and timing in the whole momentum range required for e/π, π/K and K/p separation. Such a beam test will be performed with electron and hadron beams at Fermilab in 2026, with an extensive use of first article components (outer vessel shell, aerogel, mirrors, HRPPDs).

Status of maturity of the subsystem: The design of the pfRICH subsystem is in a fairly mature state. As described in previous sections, the pfRICH consists of a cylindrical vessel with two endcap plates, an aerogel tile plane, an HRPPD sensor plane with onboard electronics, mirrors and a number of subsystems (HV and LV, cooling, gas, light monitoring). Engineering design of all of these components (except for the HRPPD ASIC backplane for the reasons stated above) is by now sufficiently advanced to be more than 60% ready by the CD-2 EIC Project phase at the end of 2025.

Environmental, Safety and Health (ES&H) aspects and Quality Assessment (QA) planning: The environmental, safety, and health impacts of the pfRICH subsystem are expected to be minimal. When installing and integrating the pfRICH into the overall detector, all applicable safety standards (i.e. OSHA, Critical Lift procedures, etc.) will be followed and adhered to. Furthermore, the composition of the vessel itself consists mainly of carbon fiber, epoxy, and plastic and any (small) excess can be retained for future use or disposed of via standard waste streams. The operation of the detector will require a modest 400 watts of cooling power and the working gas is pure nitrogen which does not pose any greenhouse concerns.

The individual HRPPDs, mirrors, and aerogel tiles used in the pfRICH will all undergo rigorous quality assessment (QA) checks to ensure that their operation and/or properties are within acceptable limits. Beyond the testing done by the manufacturer, the performance of individual HRPPDs will be evaluated using test stands located at BNL, JLab, and possibly Yale University. While the details of the test stands differ, they all consist of a light-tight enclosure to house the HRPPD, a fiber-coupled light source (either a pulsed laser or a monochromator), an optical assembly to focus the light onto the sensor, power supplies, and readout electronics, see Fig. 7 (left) as an example.

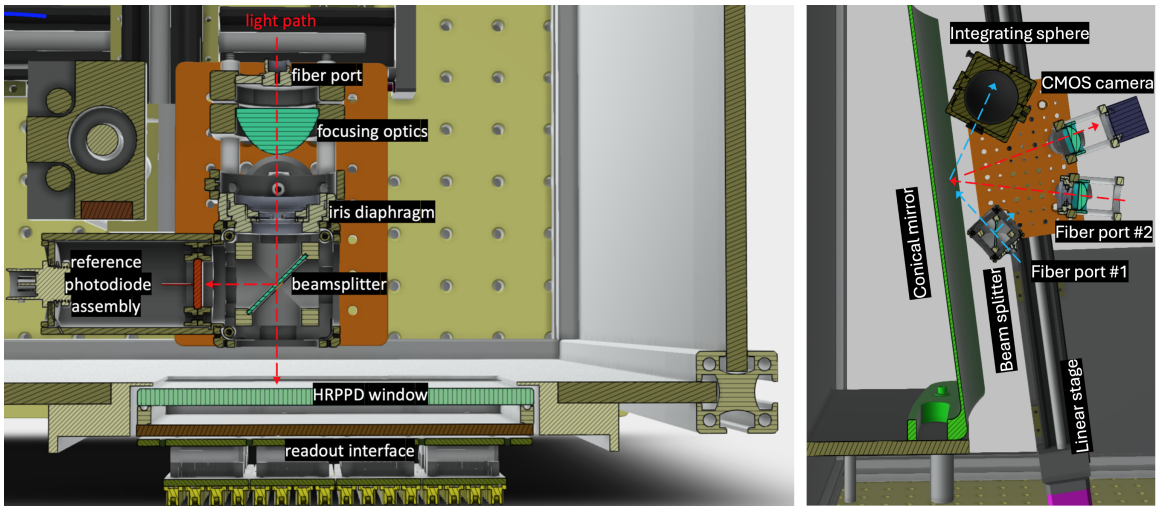

Figure 7: Left: optical setup of an existing HRPPD QA station at BNL. Right: optical table of the future full size mirror QA station at BNL. See text for more details. (Figure documentation)

The gain uniformity, quantum efficiency, photon detection efficiency, and dark count rates will be determined over the entire active photosensor area. In addition, the use of a Menlo Systems Elmo 780 femtosecond laser at BNL will allow precision determination of the timing characteristics of the sensors.

The reflectivity of the mirror samples produced at SBU will be determined using a dedicated test stand at BNL, see Fig. 7 (right). The setup will consist of a large dark box with a mirror sample stand, multi-functional optical table assembly and motion control hardware

implemented as a combination of rotary and translation stages.

Blue arrows in Fig. 7 (right) show the light path of the reflectivity measurement setup. Light from a halogen/deuterium arc lamp source located outside of the dark box will be fed via fiber with a collimating lens to a beam splitter which directs a fraction of the light to a reference photodiode and passes the remaining beam to the conical mirror sector. Reflected light gets collected in the integrating sphere and then fiber coupled into a compact spectrometer, providing a capability to measure the whole wavelength spectrum of interest at once. The reflectivity will be determined by taking the ratio of the wavelength spectra of the conical mirror under study and a calibrated small flat stock mirror located next to it. Variations in the light source intensity will be corrected using the reference photodiode.

Red arrows show the optical path of a 2D surface mapping setup. A monochromatic light will be directed onto a focusing lens through a single mode fiber with a few micron diameter core. The image of this point-like source after a reflection off the conical mirror surface will be focused onto a CMOS camera sensor. Transverse displacement of this image when the optical head is moving along the mirror surface in azimuthal and lateral directions is a measure of deviation of the mirror surface from an ideal conical shape.

The aerogel quality assessment will be performed at Temple University and include assessments of the refractive index, transparency, uniformity and mechanical specifications. So far, the refractive index has been determined by measuring the deflection of the light passing through the corner of the aerogel tile, following the procedure described in Ref. [17]. Work is currently underway to develop a setup and approach that is based on measuring changes in the polarization between the light incident on the aerogel and the light that is reflected from its surface. This would allow for localized refractive index measurements to ensure not only the aerogel has the proper mean refractive index, but also its uniformity across the whole tile. Transparency QA will make use of wavelength dependent transmittance measurements carried out using a newly commissioned and validated UV/VIS LED-spectrometer system. The transmittance data will be fitted with the Hunt Formula [18] to extract aerogel properties such as the scattering surface coefficient and clarity, as well as the wavelength dependent properties which include the transmittance, transmission length, and scattering length. The density will be calculated by measuring the aerogel mass using a precision scale (100 μg) and volume via caliper and touch probe. Reference jigs can be made to ensure that the aerogel mechanical specifications such as the side-to-side length, tile height, and surface planarity variations are within acceptable ranges.

Construction and assembly planning: The pfRICH has been designed such that it can be fully assembled and inserted into ePIC in one piece. Individual components such as vessel walls, sensor and aerogel planes, mirrors, HRPPDs, and aerogel tiles will be manufactured and tested at various locations and then shipped to BNL for final assembly. It is envisioned that final subsystem assembly will take place in a cleanroom or dedicated lab space within the physics building at BNL. Once assembled, the pfRICH will be transported by truck roughly 1.3 miles to the experimental hall where it will be integrated with the other ePIC subsystems.

The assembly of the pfRICH itself will proceed via the following general steps: (1) assemble the aerogel plane by fastening it to the outer and inner walls, (2) place the sub-assembly such that the upstream end is facing down, (3) add aerogel tiles and aerogel retaining system into the aerogel plane, (4) pre-assemble most of the sensor plane by affixing the inner and outer mirrors and any vessel services (i.e. inner gas tubing, laser monitoring system, etc.) to the sensor plane, (5) lift the sensor plane over the rest of the vessel and lower the sensor plane and mirrors into place, (6) fasten the sensor plane to the subassembly at the inner and outer walls, completing the cylindrical vessel, (7) systematically insert and secure the individual HRPPD modules into the back of the sensor plane, (8) lift the completed pfRICH, rotate it into its operating position, and install it onto the transportation/storage cart.

Collaborators and their role, resources and workforce: The pfRICH Detector Subsystem Collaboration (DSC) member institutions, as well as other affiliated groups are listed in Tab. 2, along with their anticipated commitments.

Table 2: Institutions contributing to the pfRICH effort and their roles, resources, and participating workforce. Starred entries indicate no institutional commitment.

Institution	Role	Workforce	Resources
Brookhaven National Lab	Project Lead HRPPD and mirror testing Gas Systems DAQ Detector and physics simulation	5 staff	HRPPD test stands (pico/femtosecond laser, dark box with translation stages, high-performance scope, waveform digitizers) Mirror test stands (monochromator, spectrometer) Sample temperature control chamber
Chiba University*	Connection to aerogel factory	N/A	Aerogel production equipment
Duke University	Detector modeling	1 staff	
INFN Genova*	HRPPD B-field studies	1 staff	
INFN Trieste*	Detector modeling HRPPD aging and B-field studies	1 staff	HRPPD test stand (laser, dark box, waveform digitizers)
Jefferson Lab*	Mechanical design EIC Project support HRPPD testing	2 staff	HRPPD test stand (laser, dark box, translation stages, digitizers)
Ljubljana University & JSI*	Expert input on detector design	N/A	
Mississippi State University	Laser monitoring system	1 staff, students	
Purdue University	Vessel and mirror fabrication	2 staff, students	Machine shop and fabrication lab
Stony Brook University	Vessel fabrication Mirror coating	1 Post-doc, students	Mirror coating chamber Vessel form
Temple University	Aerogel testing and QA	1 staff	Aerogel test stand
University of Debrecen	HRPPD backplane design and fabrication	1 staff	
University of Glasgow	MCP-PMT evaluation	1 staff, students	MCP-PMT test stand (laser, dark box, cosmic ray stand, electronics)
Yale University	Software support HRPPD QA	1 staff, students	HRPPD test stand (dark box with translation stages, digitizers)

Risks and mitigation strategy: A number of risks has been identified in the past, and mitigation strategies developed.

A reliable large area highly pixelated photosensor with a high quantum efficiency and single photon timing resolution better than ∼50 ps is a core component of the pfRICH design. The pfRICH team, together with the EIC eRD110 consortium (Photosensors) has been routinely working with one of the two manufacturers remaining on the market (Incom Inc.) for several years to help the company re-design their HRPPD sensors so they fully meet EIC specifications. The ongoing evaluation of the first seven EIC HRPPDs produced in 2024 shows that overall quality, as well as reproducibility of parameters verified so far (quantum efficiency in particular) meet the requirements. As a fallback photosensor solution, we consider Photek Auratek MCP-PMTs. Such a PMT has been ordered already, and its performance will be evaluated against the pfRICH detector needs in FY25.

Aerogel tiles of required quality can be produced in a very few places worldwide. The pfRICH team, together with the EIC Project, has been routinely working with the Aerogel Factory in Japan over the last two years, to make sure the quality and production capacity meet our requirements. A technical lead of the Chiba Aerogel Factory in Japan is also a member of the pfRICH DSC, see Tab. 2. Our simulations show, that in case Aerogel Factory cannot produce sufficiently large tiles to cover the whole front wall of the vessel in a configuration with three radial bands as shown in Fig. 1, one can resort to using tiles of a readily available size up to 145 mm in a four-band configuration, with an acceptable loss of performance caused by additional dead area introduced by an extra row of radial spacers between the tiles.

Additional Material

Aerogel Test Procedures For optimal detector performance aerogel tiles must possess homogeneous refractive index, transparency, density, and thickness. We plan to carry out several measurements to ensure the quality of each aerogel tile meets the needs of the pfRICH detector.

The refractive index n can be measured using the so-called Fraunhofer method. The Fraunhofer method is a straightforward and precise technique for determining the refractive index of transparent materials, including aerogel tiles. It involves measuring the angle of deviation of light passing through a prism-shaped aerogel tile. Figure 8 shows the experimental setup used for measuring the refractive index. The aerogel tile is placed on a turntable and light from a laser source is incident on the tile. The tile is rotated until the deflection angle θ_{out} reaches a minimum. When at the minimum deflection angle, the refractive index is given by:

$$n = \sin\left(\frac{\beta + \theta_{out}}{2}\right) / \sin\left(\frac{\beta}{2}\right), \tag{1}$$

where β is the angle making up the corner of the aerogel tile ($\approx 90^o$). The deflection angle is determined by measuring the laser spot displacement x a distance L from the aerogel. The refractive index is measured using each of the four aerogel corners and then averaged together for a final nominal value.

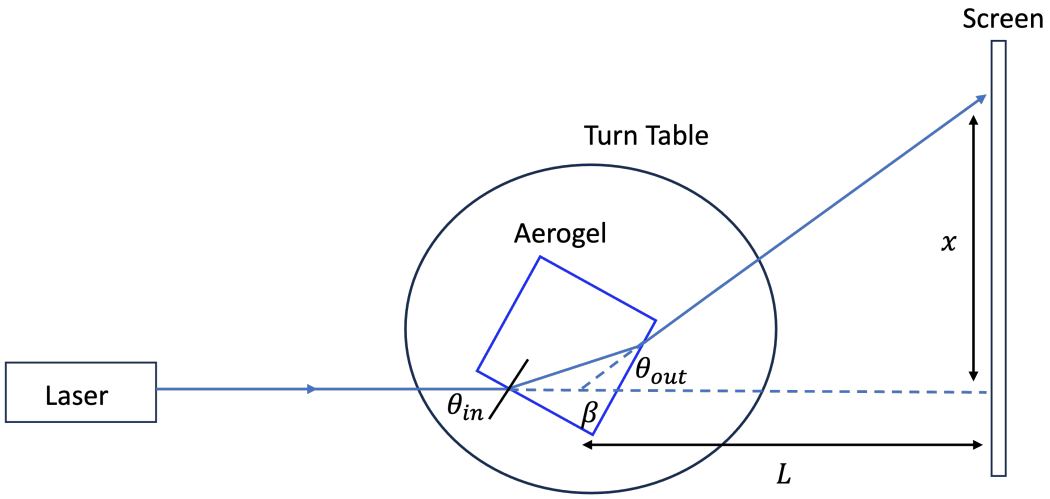

Figure 8: Block diagram of refractive index measurement via the Fraunhofer method.

The Fraunhofer method can only be used if the aerogel tiles have optical quality edges. However, it is anticipated that the final pfRICH production tiles will be water-jet cut from a bulk aerogel piece, resulting in non-optical quality edges and rendering the Fraunhofer method non-applicable. As a result we are developing another method to measure based on the change in the polarization between the incident and reflected light. This method would also allow for localized refractive index measurements across the aerogel tiles.

The aerogel's transmittance is measured across the ultraviolet (UV) and visible (Vis) spectrum. The transparency is quantified by the percentage of light transmitted through the aerogel at various wavelengths. A fiber optic cable is coupled to each of the narrow wavelength LEDs and serves as the input light source. Light from the LEDs is incident on the face of the aerogel tile and the transmitted light then passes into an integrating sphere. The integrating sphere collects the light into a fiber optic that is connected to a UV/Vis spectrometer where the light intensity is measured as a function of wavelength, I_{aero}. The aerogel is placed on a stage which can move horizontally and vertically relative to the incident LED light, allowing for transmittance measurements across the surface of the aerogel. Both the aerogel, its transnational stage, and integrating sphere are contained within a dark box. The LED transmittance measurement setup is shown in Fig. 9. The measurement is repeated for each LED without the aerogel present to obtain a reference intensity, I_{ref}. Finally, a background intensity is measured by running the spectrometer with the LED sources powered off, I_{bkgd}. The transmittance for each LED is given by:

$$T_{\lambda_i} = \frac{I_{aero} - I_{bkgd}}{I_{ref} - I_{bkgd}}. \tag{2}$$

Once the transmittance is measured from several discrete LEDs, they can be plotted vs. their respective wavelengths to obtain a wavelength dependent transmittance information.

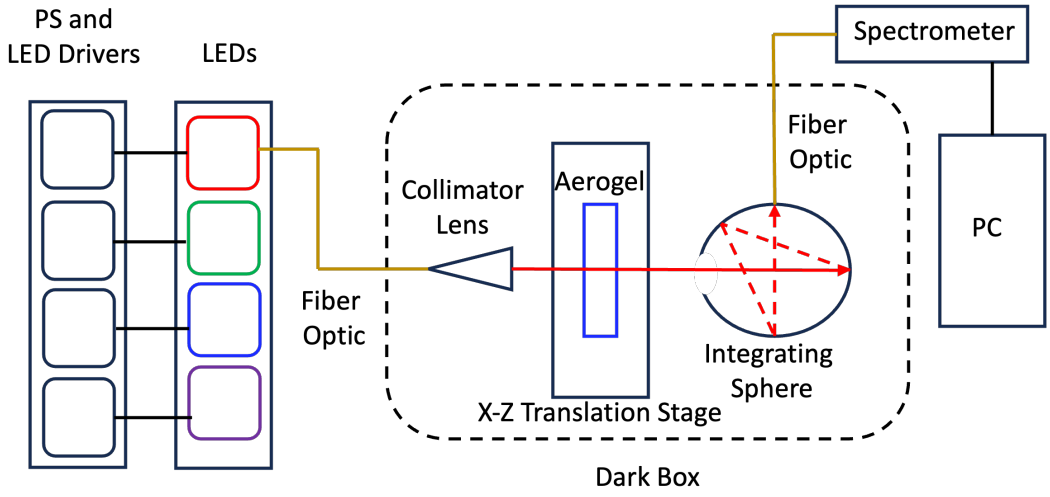

Figure 9: Block diagram of LED transmittance measurement station.

This data can be parameterized with the fit function:

$$T(\lambda) = Ae^{-\frac{Bt}{\lambda^8}}e^{-\frac{Ct}{\lambda^4}}, \tag{3}$$

where A, B, and C are the fit parameters, t is the thickness of the aerogel tile, and λ is the wavelength of the impinging light. The parameter A is known as the scattering surface coefficient, and C is the clarity factor.

The fit parameters in Eq. 3 can be used to extract properties like the transmission (Λ_{trans}), absorption (Λ_{abs}), and scattering (Λ_{scat}) lengths through the Hunt formula:

$$T(\lambda) = e^{-\frac{t}{\Lambda_{trans}}} = e^{-t\left(\frac{1}{\Lambda_{abs}}+\frac{1}{\Lambda_{scat}}\right)}. \tag{4}$$

From Eqs. 3 and 4:

$$\Lambda_{trans} = -\frac{t}{ln(A)}, \quad \Lambda_{scat} = \frac{\lambda^4}{C}, \quad \Lambda_{abs} = \frac{t\lambda^8}{Bt - \lambda^8 ln(A)} \tag{5}$$

Using the fit parameters, one can plot as a function of the wavelength the extracted transmission, absorption, and scattering lengths. One can also extract the various lengths and transmittance at a fixed wavelength for quick QA comparisons across different tiles.

An LED based transmittance station was built and commissioned at Temple University,Fig. 10. The setup consists of four LEDs of different wavelengths(340 nm, 430 nm, 530 nm, and 625 nm) providing four discrete transmittance measurements. Each LED has its own power supply and LED driver unit. The LED light is transported through a 600μm diameter fiber optic cable, with one end coupled to the LED and the other to a collimating lens. The collimated light is incident on an aerogel sample that is place about 3 cm from the

lens, and has a beam spot of about 3 mm. The transmitted light has a beam spot diameter of about 10 mm when enters it enters the integrating sphere positioned about 12 cm from the aerogel. The integrating sphere inner walls are highly reflective PTFE material and has an opening port diameter of about 2.5 cm. The light entering the integrating sphere reflects off the inner walls until it enters a 200μm diameter fiber optic that couples the integrating sphere to a UV/Vis spectrometer. The spectrometer is connected to a PC via usb cable for analysis. The aerogel tile sits on a platform that is mounted to a vertical Al extrusion that is able to slide along the extrusion. The vertical Al extrusion is mounted to a slide stage that is installed on a horizontal Al extrusion, which allows aerogel to move perpendicular to the beam direction. This setup allows measurements to be carried out over the area of the aerogel for uniformity studies. The collimator lens, aerogel and its translation stages, and integrating sphere are contained inside of a dark box to minimize ambient light and other possible external light sources that could impact the measurement.

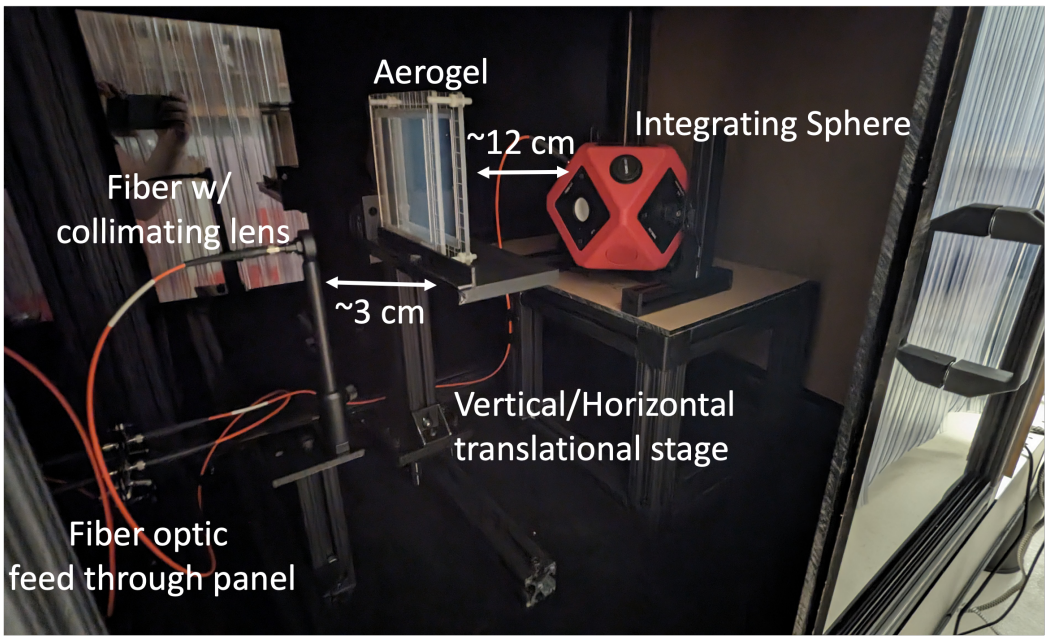

Figure 10: Inside view of the LED transmittance measurement station dark box.

Aerogel Test Results Several aerogel tiles with nominal dimensions of 11 cm $\times$ 11 cm $\times$ 2.5 cm and refractive index of 1.040, were ordered from Chiba Aerogel Factory Co., Ltd. These tiles were used to assess the optical quality of aerogel with similar properties that will be used in the pfRICH. These tiles were also used to commission and validate the QA stations that are being developed and discussed above. Table 3 lists the tiles that were used and their specifications measured by the Aerogel Factory [13].

Using the Fraunhofer method described above, the refractive index was measured using each of the four corners. Figure 11 compares the refractive index measured by Aerogel Factory and Temple University for each of the tiles. The shown refractive indices are the average of the refractive index measurements from the four corners of the aerogel tile. The

Serial Number	TSA114-3	TSA120-1	TSA120-2
Refractive Index ($\lambda = 405$ nm)	1.0377	1.0404	1.0401
Transmission Length ($\lambda = 400$ nm) [mm]	51.2	48.9	49.3
Transmittance ($\lambda = 400$ nm)	61.2	60.6	60.5
Lateral Tile Size (nominal) [mm]	109.9	109.4	110.4
Thickness (nominal) [mm]	25.1	24.5	24.8
Weight [g]	42.79	42.24	43.12
Density [g/cm^3]	0.141	0.144	0.143

Table 3: Aerogel tile specifications measured by the Aerogel Factory.

Aerogel Factory results do not have error bars applied as no uncertainty in the measurement was provided. Temple University measurements are consistent with those measured by the Aerogel Factory.

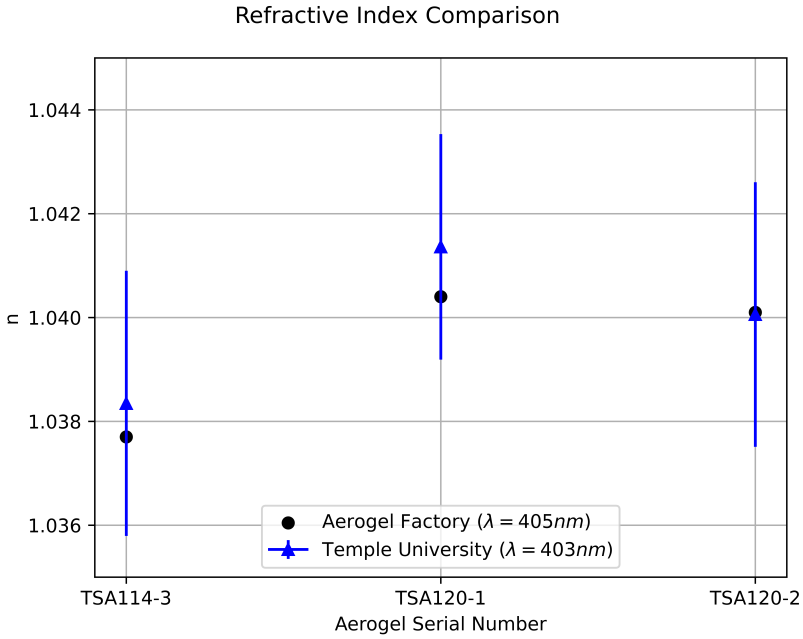

Figure 11: Refractive index measurement comparisons.

Transmittance Figure 12 compares transmittance measurements of the three aerogel tiles using different equipment. The Aerogel Factory transmittance curve (magenta) was measured by the Aerogel Factory using a Hitachi U-4100 spectrophotometer, the BNL measurements (cyan markers) were done using ..., and correspond to six different locations over the area of the aerogle tile. The black curve shows the average of the six BNL measurements. Finally, the triangle markers show the Temple University measurements performed using the LED transmittance setup. The Temple University measurements represent the average of nine measurements taken across the area of the aerogel tile. The results show consis-

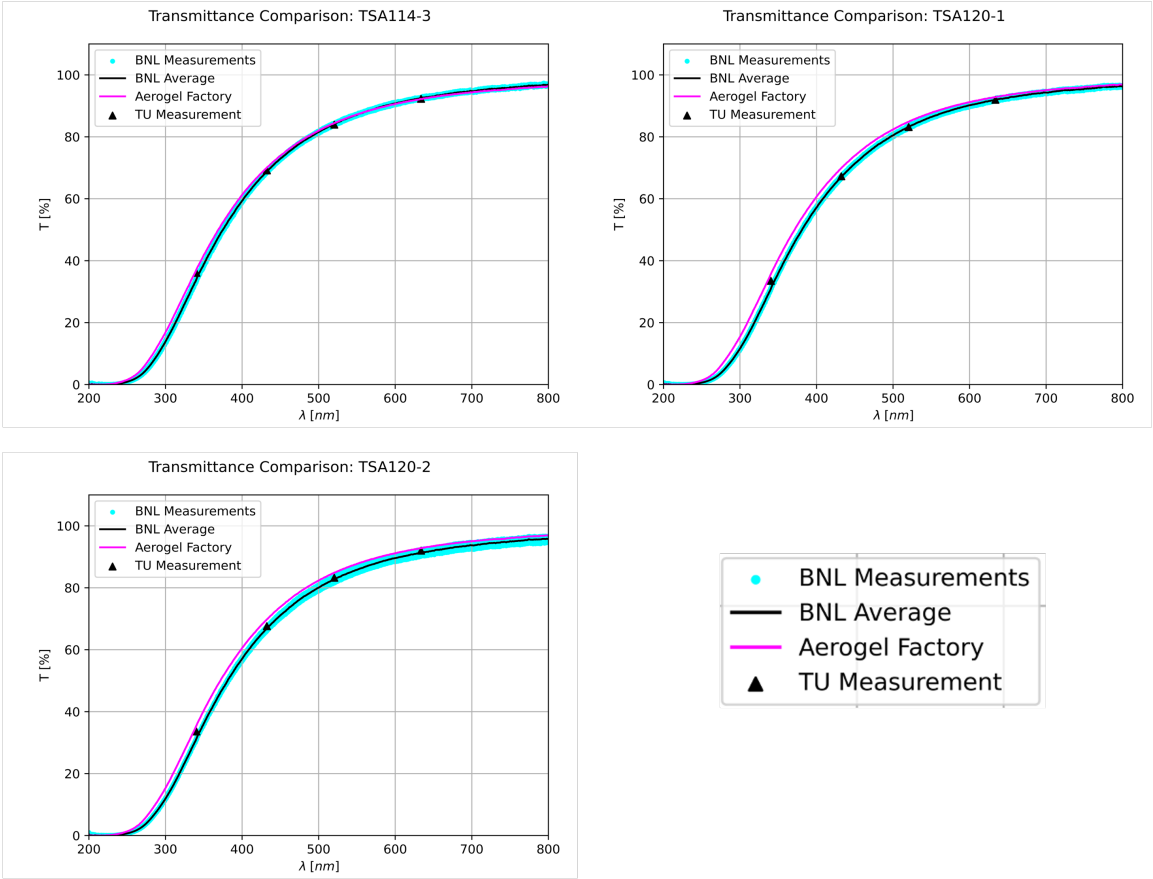

Figure 12: Transmittance measurement comparisons.

tency across the three measurement setups.

The transmittance measurements can be fit with the function defined in Eq. 3 to extract the fit parameters A, B and C. These fit parameters can be used to assess the quality of the aerogel. The parameter A represents the aerogel transparency, B is related to the light absorption of the aerogel, and C is related to Rayleigh scattering in the aerogel, or its clarity. An optimal quality aerogel tile will have an A value near 1 and small or near zero C value. Since the LED based transmittance setup only has four data points, to ensure that the function can accurately describe the limited data set, the Aerogel Factory and BNL measurements were used. The fit parameters were determined from fitting all data points across the wavelength range and compared to a fit using only the four data points that matched the wavelengths used in the Temple measurements (e.g. $\lambda = 340.5$ nm, 432.4 nm, 520.5 nm, 633.8 nm). The fit parameters determined using the full and partial data sets from the Aerogel Factory and BNL were found to be comparable and can be found in Tables 4- 6, along with the fit results from the Temple measurements. Going from using a full dataset to a partial one results in increasing the fit parameter uncertainty. We also see that the contribution from absorption (e.g. the B fit parameter) provides only a small contribution to the overall transmittance curve as it's central value is on the order

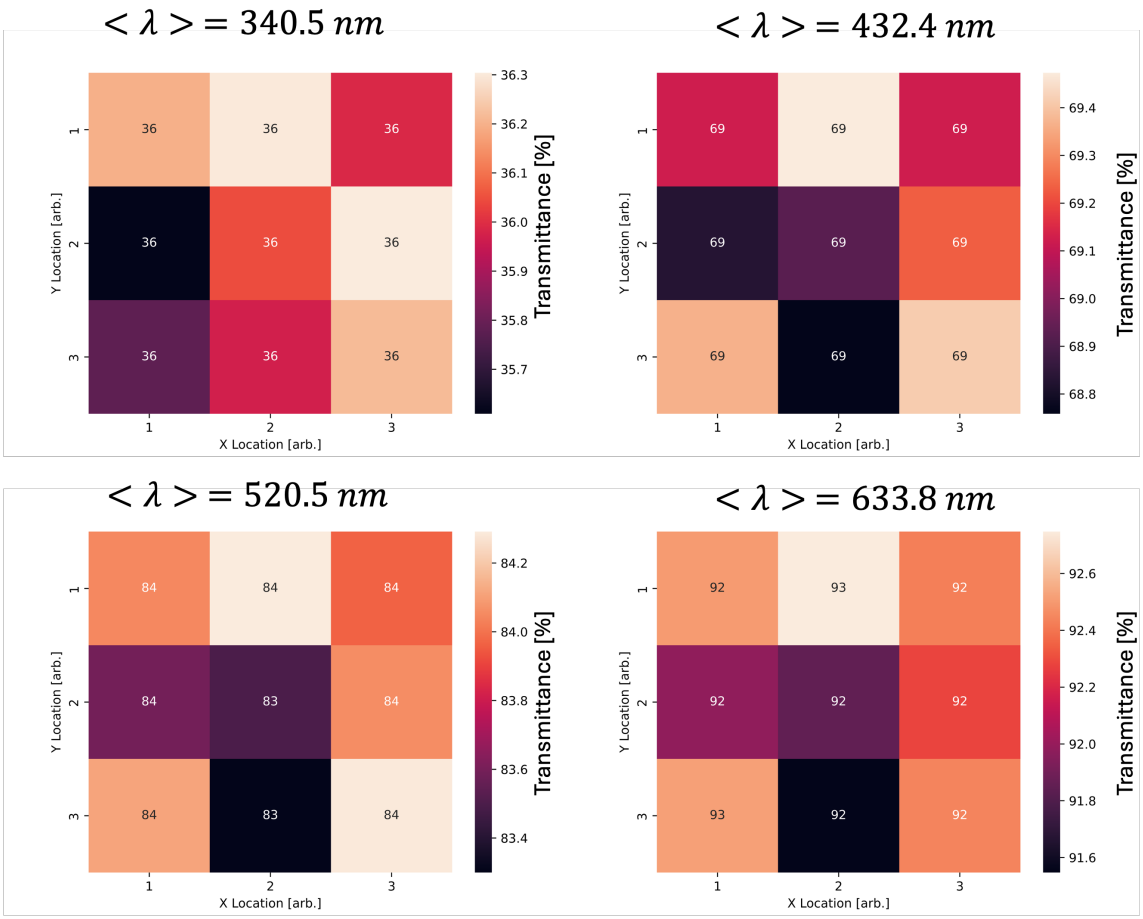

Figure 13: Localized transmittance measurements for aerogel tile TSA114-3 for different wavelengths: $< \lambda >= 340.5$ nm (upper left), 432.4 nm (upper right), 520.5 nm (lower left), 633.8 nm (lower right).

of $10^{-5} - 10^{-6} \mu m^8$.

The fit parameters can be used to determine transmission and scattering lengths, as described in Eq. 5. Figure 14 compares the transmission (top row) and scattering (bottom row) lengths extracted from the Aerogel Factory (blue band), BNL (green band), and Temple University (red band) partial datasets. Tables **??** compares the transmittance and transmission lengths at 400 nm. The Aerogel Factory Spec. row corresponds to the value printed on each of the aerogel tiles. The other values are extracted from fits to the transmittance measurements.

Mirrors Mirrors are critical in the technical design of the pfRICH subdetector system, where edge acceptance and mechanical gaps can be largely recovered by high reflective mirrors. Within the pfRICH system, there are three types of mirrors - outer, inner, and small pyramid mirrors.

Measurement	Data Set	A [%]	B $[\mu m^8/cm]$	C $[\mu m^4/cm]$
Aerogel Factory	Full	99.05 ± 0.062	$9.14 \times 10^{-6} \pm 2.51 \times 10^{-7}$	$4.57 \times 10^{-3} \pm 2.17 \times 10^{-5}$
Aerogel Factory	Partial	99.05 ± 1.59	$9.28 \times 10^{-6} \pm 6.97 \times 10^{-6}$	$4.55 \times 10^{-3} \pm 5.42 \times 10^{-4}$
BNL	Full	99.77 ± 0.09	$1.25 \times 10^{-5} \pm 4.26 \times 10^{-7}$	$4.82 \times 10^{-3} \pm 3.37 \times 10^{-5}$
BNL	Partial	99.73 ± 1.61	$1.29 \times 10^{-5} \pm 7.19 \times 10^{-6}$	$4.81 \times 10^{-3} \pm 5.50 \times 10^{-4}$
Temple U.	Partial	99.55 ± 1.60	$7.64 \times 10^{-6} \pm 7.07 \times 10^{-6}$	$4.87 \times 10^{-3} \pm 5.47 \times 10^{-4}$

Table 4: Comparison of Aerogel Factory, BNL, and Temple fit parameters for tile TSA114-3.

Measurement	Data Set	A [%]	B $[\mu m^8/cm]$	C $[\mu m^4/cm]$
Aerogel Factory	Full	99.92 ± 0.063	$1.10 \times 10^{-5} \pm 2.80 \times 10^{-7}$	$4.79 \times 10^{-3} \pm 2.32 \times 10^{-5}$
Aerogel Factory	Partial	99.86 ± 1.60	$1.21 \times 10^{-5} \pm 7.21 \times 10^{-6}$	$4.74 \times 10^{-3} \pm 5.56 \times 10^{-4}$
BNL	Full	99.58 ± 0.09	$1.57 \times 10^{-5} \pm 5.05 \times 10^{-7}$	$5.19 \times 10^{-3} \pm 3.74 \times 10^{-5}$
BNL	Partial	99.66 ± 1.63	$1.63 \times 10^{-5} \pm 7.66 \times 10^{-6}$	$5.20 \times 10^{-3} \pm 5.76 \times 10^{-4}$
Temple U.	Partial	99.95 ± 1.63	$7.61 \times 10^{-6} \pm 7.49 \times 10^{-6}$	$5.43 \times 10^{-3} \pm 5.72 \times 10^{-4}$

Table 5: Comparison of Aerogel Factory, BNL, and Temple fit parameters for tile TSA120-1.

Measurement	Data Set	A [%]	B $[\mu m^8/cm]$	C $[\mu m^4/cm]$
Aerogel Factory	Full	99.92 ± 0.063	$1.10 \times 10^{-5} \pm 2.78 \times 10^{-7}$	$4.75 \times 10^{-3} \pm 2.30 \times 10^{-5}$
Aerogel Factory	Partial	99.93 ± 1.60	$1.22 \times 10^{-5} \pm 7.13 \times 10^{-6}$	$4.70 \times 10^{-3} \pm 5.49 \times 10^{-4}$
BNL	Full	98.93 ± 0.09	$1.47 \times 10^{-5} \pm 4.89 \times 10^{-7}$	$5.11 \times 10^{-3} \pm 3.67 \times 10^{-5}$
BNL	Partial	98.90 ± 1.62	$1.56 \times 10^{-5} \pm 7.57 \times 10^{-6}$	$5.08 \times 10^{-3} \pm 5.71 \times 10^{-4}$
Temple U.	Partial	99.76 ± 1.62	$8.90 \times 10^{-6} \pm 7.37 \times 10^{-6}$	$5.23 \times 10^{-3} \pm 5.63 \times 10^{-4}$

Table 6: Comparison of Aerogel Factory, BNL, and Temple fit parameters for tile TSA120-2.

Measurement	Transmittance [%]	Transmission Length $[cm]$
Aerogel Factory Spec.	61.2	5.12
Aerogel Factory	61.18 ± 3.77	5.11 ± 0.26
BNL	59.25 ± 3.71	4.79 ± 0.23
Temple University	59.99 ± 3.73	4.91 ± 0.24

Table 7: Comparison of Aerogel Factory, BNL, and Temple aerogel tile TSA114-3 properties at $\lambda = 400$ nm.

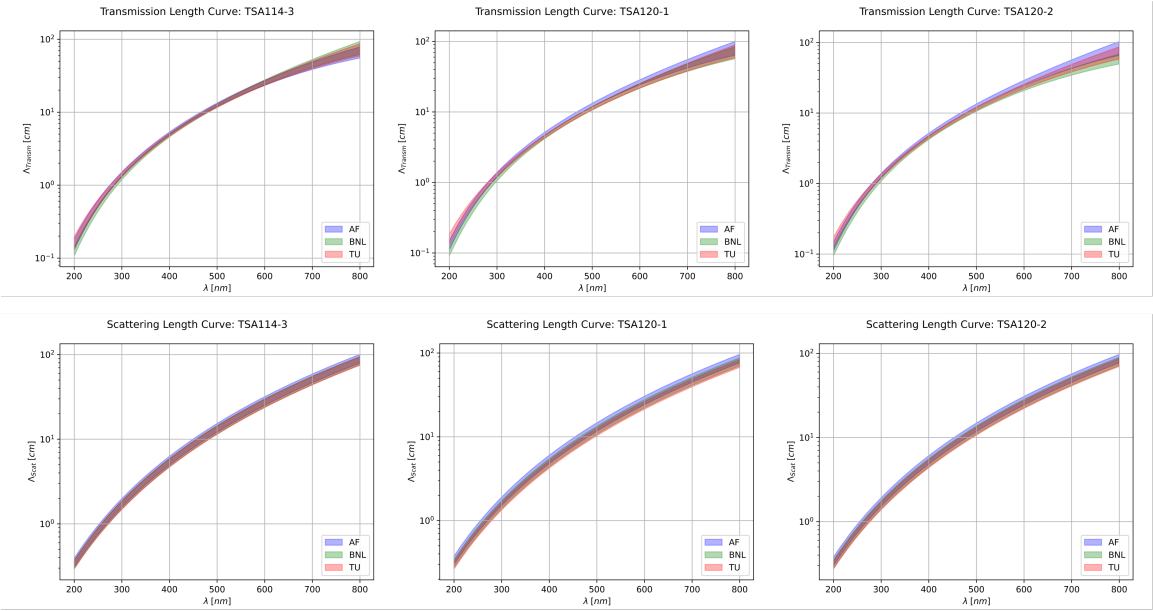

Figure 14: Comparisons of the wavelength dependent transmission (top) and scattering (bottom) lengths extracted from Aerogel Factory (blue band), BNL (green band), and Temple (red band) measurements for tiles TSA114-3 (left column), TSA120-1 (center column) TSA120-2 (right column). The width of the bands correspond to the uncertainty propagated from the fit parameters.

Measurement	Transmittance [%]	Transmission Length [cm]
Aerogel Factory Spec.	60.6	4.89
Aerogel Factory	60.63 ± 3.74	4.90 ± 0.25
BNL	57.02 ± 3.66	4.36 ± 0.20
Temple University	57.76 ± 3.67	4.46 ± 0.21

Table 8: Comparison of Aerogel Factory, BNL, and Temple aerogel tile TSA120-1 properties at $\lambda = 400$ nm.

- **Outer mirrors** are designed to reflect Cherenkov photons with large emission angles, dominated by those originating from charged particles at $\eta \approx -1.5$. There are a total of 12 sectors of conical mirrors that forms a full cylindrical mirror, which is approximately 45 cm in length and 65 cm in radius.
- **Inner mirrors** are designed to recover photons that emitted by small angle charged particles that are close to $\eta \approx -3.5$. The shape is also cylindrical and wrapped around the beam pipe and surrounding support structures.
- **Small pyramid mirrors** are placed at gaps between the HRPPD sensors to recover the photons that would go through the gaps and miss the sensor planes.

These mirrors are required to have an approximate 90% reflectivity between 300 to 600 nm

Measurement	Transmittance [%]	Transmission Length [cm]
Aerogel Factory Spec.	60.5	4.93
Aerogel Factory	60.53 ± 3.74	4.94 ± 0.25
BNL	56.99 ± 3.67	4.41 ± 0.20
Temple University	58.09 ± 3.68	4.57 ± 0.22

Table 9: Comparison of Aerogel Factory, BNL, and Temple aerogel tile TSA120-2 properties at $\lambda = 400$ nm.

in wavelength. The pfRICH team manufactures these mirrors locally at Stony Brook University by using an evaporator with mirror substrate provided by the Purdue University.

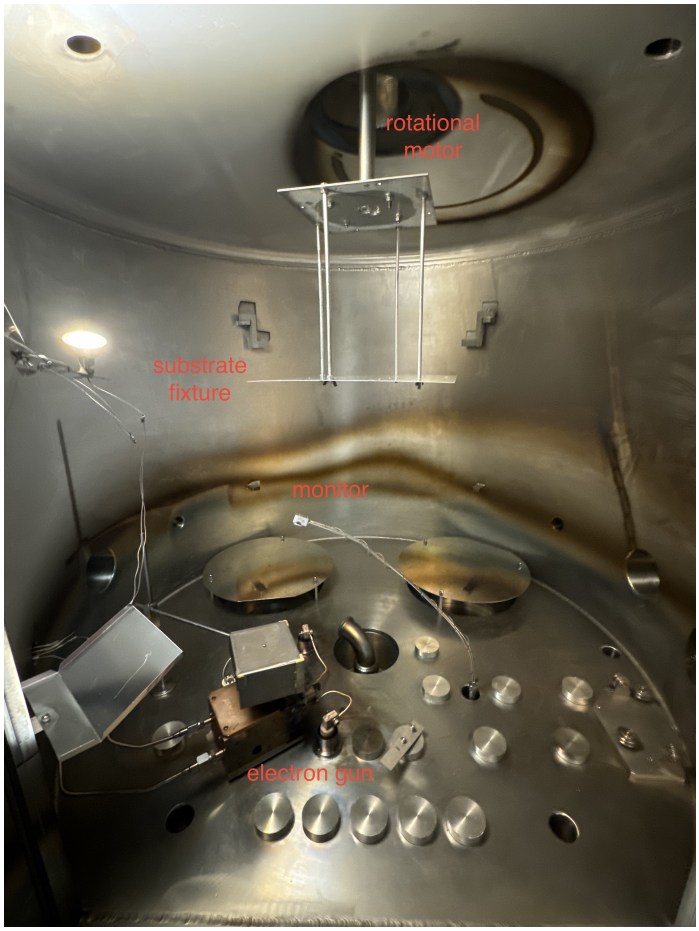

Figure 15: Evaporator for coating mirrors.

The general procedure of mirror coating is the following:

1. Substrate preparation. Purdue University collaborators use carbon fiber sheet co-bonded with Lexan to form the substrate. Epoxy is currently used for bonding the two material. Lexan as the surface material can achieve roughness approximately

down to a few nm. One of the main challenges of this step is the uniformity or surface smoothness after the co-bonding procedure.

2. Evaporation. The substrate is coating with one layer of Chromium and one layer of Aluminium in an evaporator, which is operating under vacuum. See Fig. 16 for a picture taken inside of the chamber. The basic mechanism of the evaporation is that the metal material is heated by using an electron gun and vaporize the metal such that the vapor can stick to the mirror substrate to form a reflective layer.

3. Testing. The mirror samples after the coating are tested for their performance, e.g., material deposition, reflectivity, etc.

Figure 16: A coated mirror sample from mirror coating procedure described above.

There are a few more technical implementations that are being prepared. For example, besides an electron gun, we are also installing an ion gun, which will help the metal vapor bond with the mirror substrate better and more smoothly. This could in principle improve the mirror performance. In terms of the coating technique, we are planning to perform dielectric (SiO and/or SiO_2) coating to the existing Aluminium layer to protect the surface from oxidation.

Mirror Evaluation The evaporative coating procedure uses a combination of pumps, electron - gun, and controllers placed within a large, vacuum tight, chamber to create a precisely controlled reflective film. Mirror samples are prepared and secured to a rotating fixture above the source for uniform coverage. A roughing pump begins the coating process by pumping out air, this allows for the chamber to come down to $\approx 3 * 10^{-3}$ torr from which the turbo molecular pump engages. This process allows for the removal of convection and particles that obstruct the metal vapor being deposited upon the substrate. After reaching 10^{-6} torr, the electron gun, which serves as the heating component and source, is powered on to 6.6 kV, and an appropriate raster pattern is chosen for the base, chromium, coating. The source is covered by a shutter as the intensity of current is ramped to the desired amount. Upon removal of the shutter, deposition begins until an adequate base layer of chromium, which serves as a primer, has collected on the substrate and the electron-gun is ramped down. This process is repeated with an aluminum-filled crucible within the electron-gun until a reflective coating has developed. The chamber is subsequently brought back to atmospheric pressure and coated mirrors are removed from their fixed mount. Installation of an ion source for film granularity and uniformity will be added to the evaporation chamber for improved mirror construction.

At BNL, mirror reflectivity is tested using a sophisticated setup that includes advanced equipment from Thor Labs and custom-developed software. The mirrors are positioned on a two-dimensional rotational optical platform, which is computer-controlled to achieve high accuracy. The entire setup is enclosed within a dark box and further shielded with dark cloth to minimize external light interference, thereby ensuring precise measurements.

A monochromator, serving as the light source, provides a broad range of frequencies. For our experiments, we focus on measuring reflectivity within the 200 to 600 nanometer range, encompassing the ultraviolet and much of the visible spectrum.

Our methodology for testing mirror reflectivity involves comparing the measured current from two sources: one from the reflected beam after interaction with the mirror and the other from a direct beam with no intervening objects. By assuming the direct beam has 100% reflectivity, we can accurately determine the reflectivity of the test mirror through proportional calculations

The general formula is

$$\frac{\text{Direct}}{1} = \frac{\text{Reflected}}{\text{Reflectivity}}$$

where reflectivity represents the reflectivity of the measured mirror. This equation simplifies to:

$$\text{Reflectivity} = \frac{\text{Reflected}}{\text{Direct}}$$

To accurately quantify reflectivity, it is essential to account for background noise resulting from uncertainties in the Keithley Picoammeter and external light pollution entering the black box. A separate measurement will be conducted with the beam path blocked to

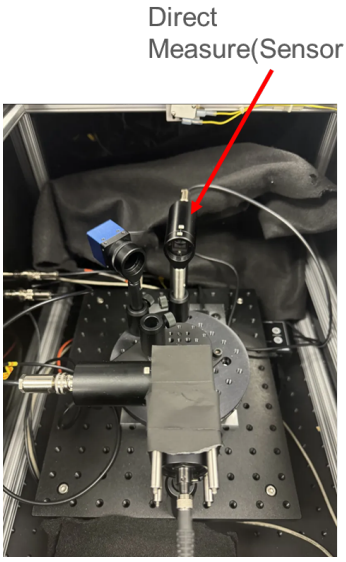

Direct measurement aim at the sensor 2. This measurement will be regarded to have 100 % reflectivity

Figure 17: Direct Measurement

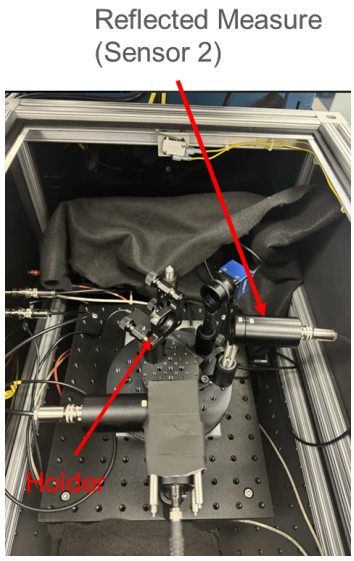

Reflected measurement with the holder in the center at 45 degree of incident

Figure 18: Reflected Measurement

determine the dark current or noise from external sources. This value will be subtracted from both the direct and reflected measurements prior to their use in the final reflectivity calculation.

To ensure consistency and minimize errors caused by fluctuations in the monochromator output, the readings are normalized by adjusting them according to their deviation from the direct measurement. This process involves using a beam splitter and an additional sensor to monitor the incident beam for both the direct and reflected measurements. The incoming beam intensities for both measurements are then scaled to ensure they have

equivalent input beam intensity before further analysis.

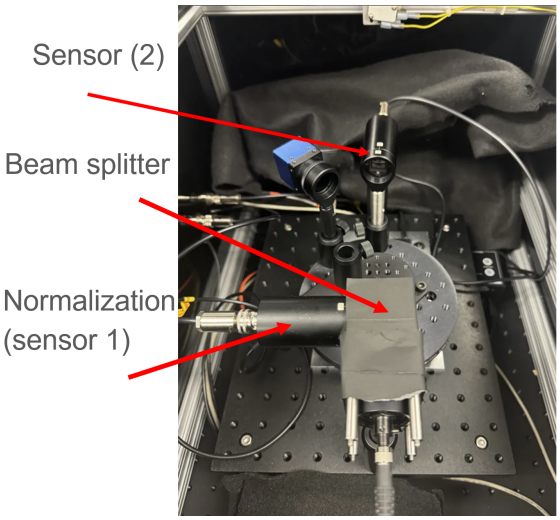

$$\text{Reflectivity} = \frac{\text{Reflected } (S_2)}{\text{Direct } (S_2)} \times \text{Scaling factor}$$

where the Scaling factor is defined as:

$$\frac{\text{Direct measurement } (S_1)}{\text{Reflected measurement } (S_1)}$$

Figure 19: Sensor 1 attached to the beam spliter on the incoming light

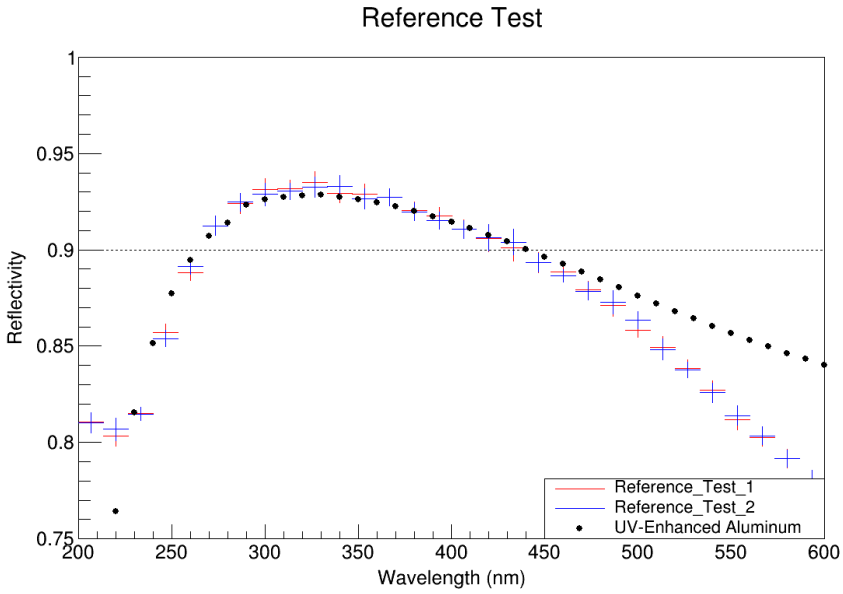

Figure 20: Comparison of BNL internal testing results with ThorLabs reference data.

Throughout the operation, realignment and reference checks were systematically conducted to ensure the accuracy and reliability of our results. Verification of our experimental setup was performed using a reference mirror provided by ThorLabs, with the specific goal of closely replicating, or ideally matching, the data points established by ThorLabs. As depicted in Figure 20, the UV-Enhanced Aluminum dotted line in black represents the measurements provided by ThorLabs. Successful replication of these data points would confirm the accuracy of our setup and methodology.

Internal testing conducted at BNL produced promising results, with our measurements closely aligning with the reference data from ThorLabs. However, our reflectivity readings showed a slight deviation from the expected values provided by ThorLabs, particularly in the wavelength range of 450 nm to 600 nm. This discrepancy may be attributed to the polarity of the light source used during the testing of the reference mirror, which could have influenced the reflectivity measurements.

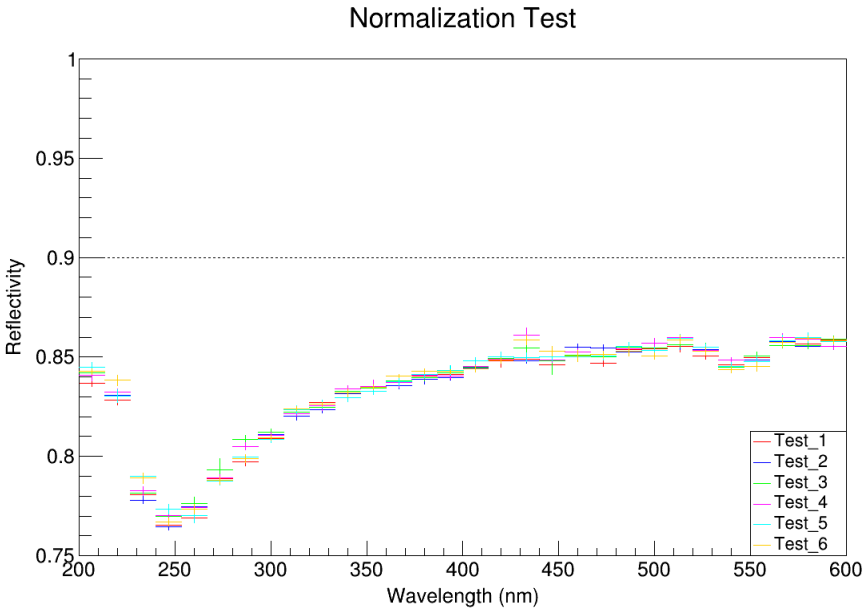

Figure 21: Results of repeated normalization tests demonstrating consistency with a maximum uncertainty of 1%.

To further assess the effectiveness of our normalization methods and evaluate the impact of minor angular deviations within the rotary stage, we conducted a series of repeated experiments. Figure 21 presents the results of six trials, in which all experimental variables were held constant, providing a comprehensive analysis of measurement deviations. The results confirm that our normalization procedure is functioning as intended.

In addition, Figure 22 depicts the micro-angle test conducted on the reference mirror, with measurements taken at five intervals, each separated by 0.2 degrees, ranging from 44.5 degrees to 45.5 degrees. The final analysis shows that the worst-case inaccuracy results in a variation of less than 0.5%. When this result is combined with the normalization process, which is designed to address instantaneous fluctuations of the monochromator, the overall uncertainty in our measurements is constrained to approximately 1%.

The current sensor configuration is designed to collect 10 data points per measurement at 30 intervals between 200 nm and 600 nm. While increasing the number of data points could potentially enhance the clarity and resolution of the data, it would also significantly extend the duration of the experiments. Careful consideration must be given to this trade-off when optimizing the experimental protocol.

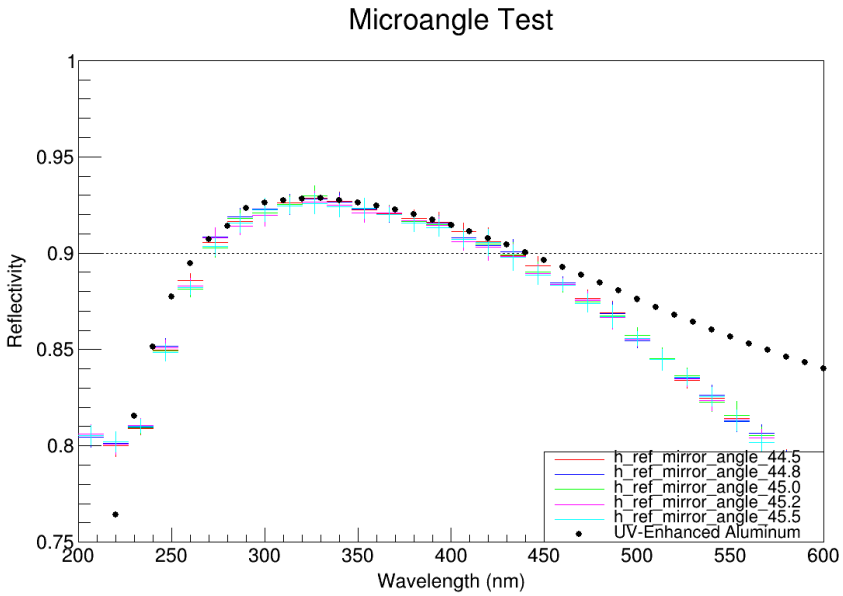

Figure 22: Micro-angle test using the reference mirror.

The test stand and procedure described above was used to evaluate the optimal aluminum deposition thickness for maximizing reflectivity. The relationship between aluminum thickness and reflectivity for several test samples is shown in Fig. 23.

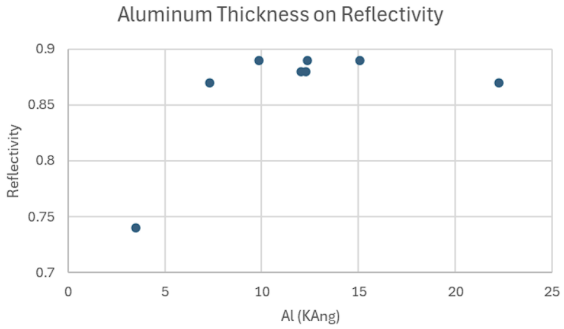

Figure 23: All coating from sample 10 to sample 16 with its reflectivity plotted against its aluminum thickness

Bibliography

[1] O. H. W. Siegmund *et al.*, "Advances in microchannel plates and photocathodes for ultraviolet photon counting detectors," *Society of Photo-Optical Instrumentation Engineers Proceedings*, vol. 81450J.

[2] C. J. Hamel *et al.*, "LAPPD and HRPPD: Upcoming Upgrades to Incom's Fast Photosensors,"

[3] "Popecki." https://indico.cfnssbu.physics.sunysb.edu/event/265/contributions/922/attachments/261/411/LAPPD%20and%20HRPPD%20update%20EIC%20Workshop%2005-08-2024.pptx.

[4] J. A. et al, "Performance of an LAPPD in magnetic fields," *Nucl.Instrum.Meth. A*, no. 1072, p. 170122, 2025.

[5] "EICROC ASIC." https://indico.bnl.gov/event/18539/contributions/73731/attachments/46348/78403/CdLT_EICROC_6mar23.pdf.

[6] "Organization for Micro-Electronics desiGn and Applications." https://portail.polytechnique.edu/omega/.

[7] J. Anderson *et al.*, "FELIX: a PCIe based high-throughput approach for interfacing front-end and trigger electronics in the ATLAS Upgrade framework," *JINST*, vol. 11, no. 12, p. C12023, 2016.

[8] "Chiba Aerogel Factory Co., Ltd.." https://www.aerogel-factory.jp/.

[9] M. Yonenaga *et al.*, "Performance evaluation of the aerogel RICH counter for the Belle II spectrometer using early beam collision data," *Prog. Theor. Exp. Phys.*, no. 093H01, 2020.

[10] S. Agostinelli *et al.*, "GEANT4—a simulation toolkit," *Nucl. Instrum. Meth. A*, vol. 506, p. 250, 2003.

[11] "ePIC IRT Package." https://github.com/eic/irt/tree/pfrich.

[12] R. Brun and F. Rademakers, "ROOT - An Object Oriented Data Analysis Framework, Proceedings AIHENP'96 Workshop, Lausanne," *Nucl. Inst. & Meth. in Phys. Res. A*, no. 389, pp. 81–86, 1997.

[13] M. Tabata, I. Adachi, Y. Hatakeyama, H. Kawai, T. Morita, and T. Sumiyoshi, "Large-area silica aerogel for use as cherenkov radiators with high refractive index, developed by supercritical carbon dioxide drying," *The Journal of Supercritical Fluids*, vol. 110, pp. 183–192, 2016.

[14] "CAEN A1515BV 16-channel floating ground High Voltage module." https://www.caen.it/products/a1515b/.

[15] "CAEN SY4527 High Voltage mainframe." https://www.caen.it/products/SY4527/.

[16] "Wiener Mpod Low Voltage system." https://www.wiener-d.com/power-supplies/mpod-lv-hv/.

[17] A. Buzykaev, A. Danilyuk, S. Ganzhur, E. Kravchenko, and A. Onuchin, "Measurement of optical parameters of aerogel," *Nuclear Instruments and Methods in Physics Research Section A: Accelerators, Spectrometers, Detectors and Associated Equipment*, vol. 433, no. 1, pp. 396–400, 1999.

[18] A. J. Hunt, "Light scattering for aerogel characterization," *Journal of Non-Crystalline Solids*, vol. 225, pp. 303–306, 1998.